steel research international
www.steel-research.de

Analysis of Hysteresis in the Regime Transition of Cocurrent Liquid–Gas Flow

Mahdi Saeedipour and Stefan Pirker*

The dynamics of cocurrent liquid–gas flow control the flow patterns and phase distribution inside the submerged entry nozzle (SEN) in the continuous casting. This regime transition from bubbly flow to annular flow is usually associated with a hysteresis effect that is not fully understood yet. Herein, the regime transition in an analogous liquid–gas flow is investigated using the volume of fluid (VOF) method. A downward turbulent water flow in a vertical pipe is considered as the computational domain at the top of which the gas is injected as a volumetric source in the VOF equation. By temporal variation of the gas volume rate following a linear ramp-up and then ramp-down, a transition from bubbly to annular flow and vice versa is observed. However, the transition occurs at different operation points and the numerical simulation pictures this hysteresis phenomenon. The regime transition is connected to the evolution of interfacial turbulence in each phase represented by the amount of vortical energy, that is, enstrophy. In addition, the temporal variation of different enstrophy generation/destruction mechanisms is evaluated. The hysteresis phenomenon is explained by the differences in the history of these mechanisms and the difference in the enstrophy generation level upon transition.

1. Introduction

Cocurrent liquid–gas flow occurs in a broad range of applications in chemical, mechanical, and metallurgical industries. One important application is the continuous casting process where the molten steel flows from the tundish downward to the mold through the submerged entry nozzle (SEN). This flow is usually associated with argon gas injection to prevent clogging and deal with small impurities. Depending on the ratio of argon and steel flow rates, the two-phase flow can encounter different regimes from a bubbly flow to an annular flow. The latter should be prevented in a sustainable steel production line,[1] which explains the necessity to characterize and control the two-phase flow in the SEN. Fundamental studies on the liquid–gas flow in vertical downward channels have been carried out mostly on water–air systems and different regimes such as bubbly, slug, churn, and annular flows have been identified according to the gas loads, that is, ratio of mass flux of gas and mass flux of liquid and the liquid and gas superficial velocities.[2] Several studies have focused on flow characterization[3,4] and producing regime maps mostly based on experiments.[5–7] For a comprehensive review of regime maps in vertical gas–liquid flows, we refer to Wu et al.[8] and the references therein. The regime transition in cocurrent liquid–gas flow has also been the topic of several analytical and experimental studies.[9–11] Accordingly, a couple of criteria for transitions are postulated mainly based on the balance of forces acting at the interfacial region. When the volume of gas exceeds a certain level and the bubbles become densely packed, the probability of bubble coalescence increases, and thus a transition from bubbly flow to slug flow occurs.[12] Also, when the interfacial instability reaches a point that the surface tension cannot balance the inertial force of the large gas structure, an annular flow is established.[13] Although some studies have used different expressions to explain the transition phenomenon (e.g., in terms of the pressure difference between gas and liquid[14]), it can be concluded that the local energy balance between interacting inertia and surface tension effects is the central concept in most of previous studies.

The focus of the present study is on a phenomenon that is less discussed in the existing literature: the hysteresis of regime transition in cocurrent liquid–gas flows with varying operating conditions. To the authors' best knowledge, Maruyama et al.,[15] first reported this phenomenon in their experimental analysis of flow transition in bubble columns. Later and in the context of SEN flow, Planquart et al.,[1] carried out a set of measurements using water–air facilities and reported a hysteresis effect during regime transition. In their experiments, they first established a bubbly flow. Then, by increasing the air flow rate in the vertical channel, they could observe that the transition from bubbly flow to annular flow starts at a certain gas flow rate until an annular flow is established. Then, they decreased the air flow injection with a similar decreasing rate. However, the transition

M. Saeedipour, S. Pirker
Department of Particulate Flow Modelling
Johannes Kepler University
Linz A-4040, Austria
E-mail: mahdi.saeedipour@jku.at

The ORCID identification number(s) for the author(s) of this article can be found under https://doi.org/10.1002/srin.202100800.

DOI: 10.1002/srin.202100800

from the annular flow to the bubbly flow did not occur at the expected gas flow rate that occurred during the increasing mode. Nevertheless, the physical reasons remain unexplained in their work. Since then, this interesting observation and possible explanations for that have been less investigated. Recently, Thumfart et al.[16] have observed similar phenomena in their 1:3 water model experiments, where the phase distribution changes hysterically by changing the gas flow rate during the increasing and decreasing operation. In the present study, we intend to investigate this phenomenon using computational fluid dynamics (CFD) simulations and further explore the physics resulting in hysteresis occurrence. We consider an analogous water–air model and use the volume of fluid (VOF) method to track individual interfacial structures (e.g., bubbles) and their interactions with the flow turbulence that eventually result in the transition from bubbly regime to slug and annular flow. Given the limitations to resemble the complex flow configuration in real-scale SEN, we utilize a coflow setup that consists of a vertical pipe with a turbulent liquid inlet, at the top of which we inject gas with a temporally varying rate. Even though this might seem an oversimplification of a complex process, this setup could provide a computational platform to realize the ramp-up and ramp-down stages and serves as a workable case for fundamental analysis of the liquid–gas regime transition. In the following sections, we first present the simulation method. Then, we elaborate on the simulation setup followed by Results and Discussions. We base our investigation on the domain-integrated quantities obtained by CFD simulation and connect the regime transition to the evolution of interfacial turbulence by analyzing the energy in the turbulent structures and the mechanisms that contribute to the distribution of vortical energy (enstrophy) in each phase. Such macroscopic analysis is of high relevance for phase distribution monitoring in the SEN during continuous casting.

2. Modeling and Simulation

2.1. Governing Equations and Simulation Method

The fluid dynamics of interfacial flows such as gas bubbles in water can be described by the governing equations of two-phase incompressible flow in the context of one-fluid formulation comprising the continuity and Navier–Stokes equations together with the transport equation for the VOF as follows.

$$\nabla \cdot \mathbf{U} = 0 \tag{1}$$

$$\frac{\partial(\rho \mathbf{U})}{\partial t} + \nabla \cdot (\rho \mathbf{U} \otimes \mathbf{U}) = -\nabla p + \nabla \cdot (2\mu \mathbf{D}) + \rho \mathbf{g} + \mathbf{F}_\sigma \tag{2}$$

$$\frac{\partial \alpha}{\partial t} + \nabla \cdot (\alpha \mathbf{U}) = S_\alpha \tag{3}$$

In this system of equations, $\mathbf{U}$ is the mixture velocity vector shared with both phases. p is the pressure and $\mathbf{D} = \frac{1}{2}[(\nabla\mathbf{U}) + (\nabla\mathbf{U})^{\mathrm{T}}]$ is the rate of deformation tensor. The VOF scalar function α is used to determine the density and viscosity of the flow based on a mixture assumption as $\rho = \alpha\rho_1 + (1-\alpha)\rho_2$ and $\mu = \alpha\mu_1 + (1-\alpha)\mu_2$. The surface tension force, $\mathbf{F}_\sigma$, is computed by the continuous surface force (CSF) method.[17] In this approach a basic definition of interface normal vector is applied using the gradient of VOF function; then, the unit interface normal and its curvature are determined as $\widehat{\mathbf{n}} = \nabla\alpha/|\nabla\alpha|$ and $\kappa = -\nabla \cdot \widehat{\mathbf{n}}$, respectively. Using these two quantities, the surface tension force reads $\mathbf{F}_\sigma = \sigma\kappa\widehat{\mathbf{n}}\delta_s$, where σ is the surface tension coefficient and $\delta_s \equiv |\nabla\alpha|$ is the mathematical delta function that tends to infinity at the interface and zero elsewhere.

The source term S_α on the right-hand side of Equation (3) is usually zero unless there exists phase change or mass source in the system. In the present study, we consider the latter to inject air in the liquid flow, which is discussed later. This set of equations could picture a highly resolved description of the interfacial physics such as bubble dynamics and interface motions if sufficiently high grid resolutions are provided and correct numerical algorithms are used. To solve the abovementioned system of equations, we use the geometric VOF approach of IsoAdvector,[18] which is officially released as the interIsoFoam solver within OpenFOAM-v2006 software package and the next releases. For further details about the method and numerical setup, we refer to other studies.[19,20]

2.2. Simulation Setup

To investigate the transition of cocurrent flow, a simulation setup with temporally varying air volume flow rate is proposed. A 3D pipe of $H = 0.3$ m and $D = 0.023$ m is considered as the computational domain, to be compatible with the size of SEN geometry in the 1:3 water model of Thumfart et al.,[16] as depicted in **Figure 1**. Note that in the water model gas is introduced through a centric hole in the stopper in alignment with the axis of the SEN. The air and water material properties are set according to the standard conditions ($\rho_w = 1000\,\mathrm{kg\,m^{-3}}$, $\rho_a = 1\,\mathrm{kg\,m^{-3}}$, $\mu_w = 1\mathrm{e}\text{-}3\,\mathrm{Pa \cdot s}$, and $\mu_a = 1.5\mathrm{e}\text{-}5\,\mathrm{Pa \cdot s}$), and the surface tension coefficient is $0.072\,\mathrm{N\,m^{-1}}$. The domain was discretized with structured grids with two different resolutions of G-1 (N= 270 296, $\Delta_{min} = 3.3\mathrm{e}\text{-}4$ m) and G-2 (N= 740 775, $\Delta_{min} = 2.8\mathrm{e}\text{-}4$ m). The inlet and outlet boundaries are located at the top and bottom of the domain surrounded by domain walls where typical inflow, outflow, and wall boundary conditions are imposed. The simulation boundary conditions for volume fraction, velocity, and pressure fields are summarized in **Table 1**. It should be further noted that these boundary conditions are the existing implementations of classical Dirichlet, Neumann, and Robin boundary conditions in OpenFOAM terminology. For further explanation, we refer to OpenFOAM user guide.[21]

To establish a workable simulation setup for the downward cocurrent flow of water and air, two possibilities exist: 1) two parallel inlets for each phase at the upper plane and 2) a single inlet for one phase while introducing an explicit volumetric mass source for the other phase inside the domain. Option (1) would be challenging to adopt due to the complexity of defining proper inflow conditions for each inlet, as well as the formation of a mixing layer between the phases upon entering the domain. Following option (2), the upper plane is set as the inlet for the water phase, and a subregion slightly below the inlet patch to inject a time-varying volumetric source of air into the domain

steel research international
www.steel-research.de

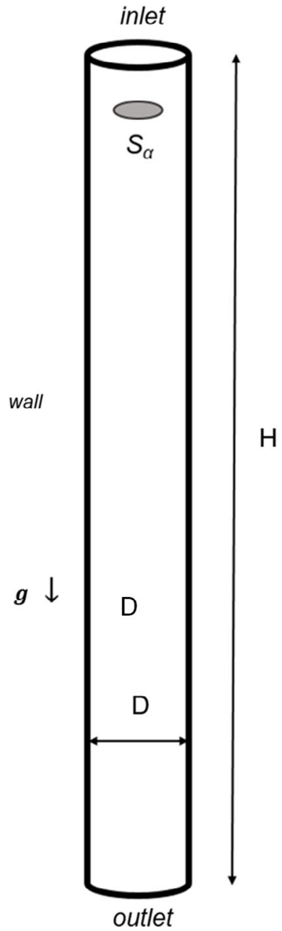

Figure 1. Schematics of the computational domain and boundary conditions.

(as shown in Figure 1). To be consistent with the range of flow rates reported in the one-third water model experiments of Thumfart et al.,[16] a fixed volume flow rate of $Q_w = 3.8\text{e-}4\,\text{m}^3\,\text{s}^{-1}$ for water (resulting in $Re = 20\,800$) and a varying volume flow rate of $Q_a = 2\text{e-}5$ to $9\text{e-}5\,\text{m}^3\,\text{s}^{-1}$ are assumed for air. It has to be noted that the entire pipe is initially filled with water, and a turbulent velocity profile with 10% fluctuations is imposed as the inlet boundary condition corresponding to Q_w.

To account for the air flow, a circular subregion with a diameter of 0.01 m and one-cell layer thickness is chosen to inject the volumetric source of air into the domain corresponding to Q_a. Numerically, it is done by determining the term S_α in Equation (3) for entire computational cells located in this subregion to act as a negative source term for water volume fraction and generate air bubbles. The maximum and minimum values of S_α are computed based on the intended maximum and minimum gas flow rates, that is, $Q_a = 2\text{e-}5$ to $9\text{e-}5\,\text{m}^3\,\text{s}^{-1}$. In fact we carried out several test simulations to determine the range of S_α and concluded that S_α must vary between 200 and $1200\,\text{s}^{-1}$ (with negative sign) to represent the ramp-up and ramp-down phases within the intended air flow rates. It should be mentioned that in this numerical setup the ramp-up and ramp-down phases (i.e., the linear variation of S_α) could occur with different slopes, and the gentler the slope, the longer the ramp-up and ramp-down phases would take. To avoid long simulation runs, we chose a slope of 200, as shown in **Figure 2**. Therefore, to let the first generated bubble thread reach the end of the pipe and disregard the initial unsteady effects, each simulation was initially run for 1 s with the lowest S_α. Then, the ramp-up stage occurs for $1 < t < 6$ s, followed by a ramp-down stage for $6 < t < 11$ s, as presented in Figure 2. This constitutes a workable coflow setup with varying operating conditions. It should be noted that a complementary test simulation with the slope of 100 was also carried out (not presented here) and the results reveal a similar trend. Thus, we proceed with the current setup for the analysis of the cocurrent flow.

Table 1. The boundary conditions for different quantities of the simulation setup in the context of OpenFOAM.

Boundary	Velocity [**U**]	Pressure [p]	Volume fraction [α]
Inlet	turbulentInlet	zeroGradient	fixedValue ($\alpha = 1$)
Wall	noSlip	fixedFluxPressure	zeroGradient
Outlet	pressureInletOutletVelocity	totalPressure	zeroGradient

2.3. Grid Study

Two sets of simulations were performed on both grid resolutions, and the domain-integrated kinetic energy ($K = \int_V \frac{1}{2}\rho|\mathbf{U}|^2 \mathrm{d}v$) is chosen as the measure for the grid-independence study. As demonstrated in **Figure 3**, both grids yield a similar trend for the evolution of kinetic energy. Particularly, the maximum kinetic energy is almost identical. Thus, we focus on the results obtained on G-2 in the remainder of this study. In addition, we accept that the simulation is not fully resolved. However, as the present analysis is based on macroscopic flow characteristics, we can assume that the domain-integrated quantities could still represent the global flow physics sufficiently. It has to be mentioned that no explicit turbulence model is used in this study and it is assumed that the second-order spatial discretization of the convective term in the

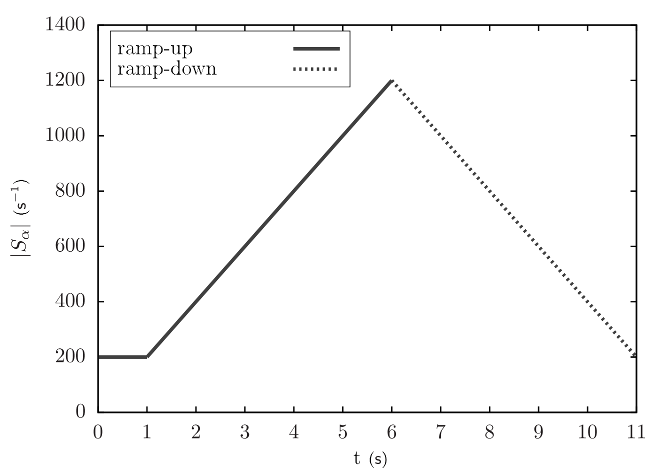

Figure 2. Temporal variation of $|S_\alpha|$ for the gas injection during the ramp-up and ramp-down phases.

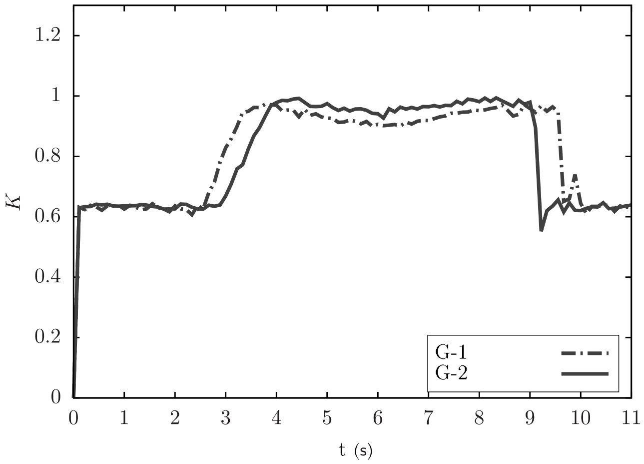

Figure 3. Temporal evolution of domain-integrated kinetic energy normalized by the maximum energy on the finest grid.

momentum equation provides the dissipation for small unresolved scales. Particularly in our previous research,[22] we have observed that such an implicit large eddy simulation (LES) approach reveals an almost similar trend to quasi direct numerical simulations (quasi-DNS) simulations for the domain-integrated enstrophy, whereas an explicit LES model of Smagorinsky could excessively induce dissipation to the turbulent flow. Thus, we leave further investigation on the proper turbulence models and small unresolved scales to future works.

3. Results and Discussion

3.1. Analysis of the Regime Transition

Having defined a workable numerical setup for the cocurrent flow, the numerical simulation of the unsteady two-phase flow during the increase and decrease in air volume flow rate was performed. **Figure 4** shows two different regimes during the ramp-up phase. Initially with a low gas flow rate, a bubbly flow is established where individual bubbles are clearly visible. By increasing the gas flow rate, the bubbles become larger with the tendency to form large slug threads, which, eventually, lead to a complete annular flow. **Figure 5**a shows the temporal evolution of the domain-integrated gas volume normalized by the pipe volume. After the initial phase, the total gas content starts to rise during the ramp-up phase due to the formation of larger bubbles and reaches in a total 10% of the domain. Shortly after $t = 3$ s, the transition begins, which results in a sharp increase in gas volume content to 42% until $t = 4.2$ s, where the annular flow is established. From this moment on, the gas content further increases but with a gentle slope until the end of the ramp-up phase at $t = 6$ s, where almost 45% of the domain is filled with gas. According to the description of the simulation setup, the ramp-down phase begins at this instant of time and total gas volume starts to decrease with the same slope. However, as evident from Figure 5a, the transition starts at a later instant of time in comparison with the ramp-up phase. In other words, the gas core remains intact for a longer period of time until the transition occurs at around $t = 9$ s, where the gas content is slightly below

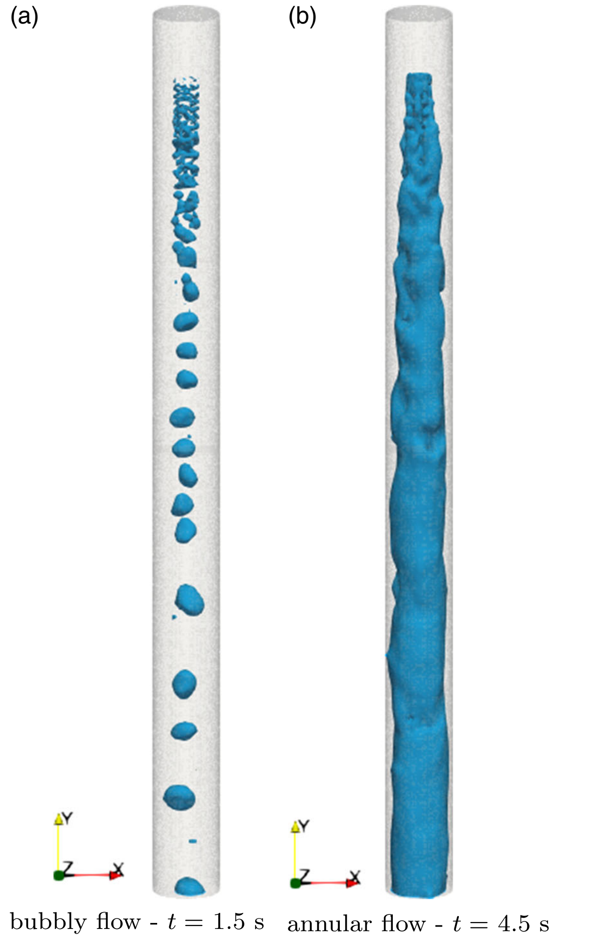

Figure 4. Snapshots of different regimes during the ramp-up phase: a) bubbly and b) annular flow. The volume of fluid isocontour of 0.5 visualizes the liquid–gas interface.

40%. It is evident that the temporal variation of total gas content does not exhibit a symmetric profile around $t = 6$ s, and the transition from annular flow to bubbly regime encounters a sort of delay. By rearranging the order of the data for $6 < t < 11$ s, and replotting them on $1 < t < 6$ s for comparison, a clear hysteresis in the transition point is demonstrated in Figure 5b.

To better understand the physics of transition, a more detailed illustration of the bubbly and annular regimes is presented in **Figure 6** by two instantaneous snapshots of interfacial structures at $t = 1.5$ and 4.5 s. The flow streamlines are colored by velocity magnitude and the vortices are visualized using Q-criterion isosurfaces. These instantaneous snapshots reveal the nature of the turbulent structures inside and outside the gas structures at each regime. While the bubble thread features a lower turbulence intensity inside the gas pockets, the vortical structures are numerous inside the gas core during the annular flow. In addition, results show that the gas bubbles are initially formed under a balance between the inertia in each phase and the surface tension forces. For the bubbly regime, the low turbulence intensity inside the gas cannot overcome the surrounding liquid, and the surface tension causes the vortical structures to be caught by the interface and forms a bubble. By increasing the gas flow rate,

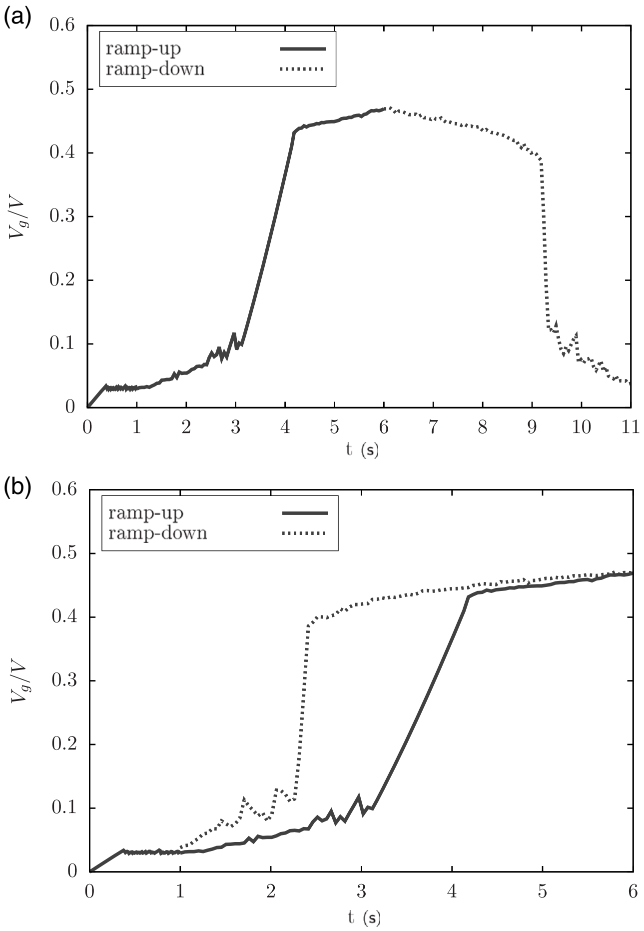

Figure 5. a) The temporal variation of normalized domain-integrated gas volume and b) the same plot with the rearranged ramp-down data, where the transition hysteresis is more evident.

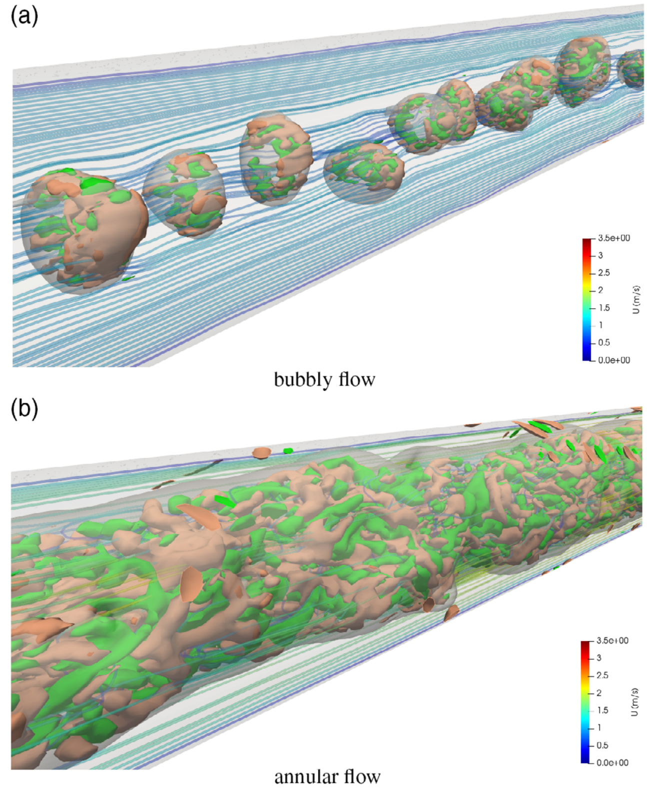

Figure 6. Instantaneous snapshots of interfacial and vortical structures for the bubbly (top) and annular (bottom) regimes. The volume of fluid isocontour of 0.5 (grey) visualizes the liquid–gas interface. The streamlines are colored by the velocity magnitude, and the vortical structures are visualized by the *Q*-criterion iso-surface of 1e5 s^{-2} (green) and −1e5 s^{-2} (light red).

the turbulent structures in gas become stronger enough to resist the surface tension effect imposed by the interface longer. This results in the formation of larger air pockets (e.g., slug structures) until the transition point. At this point, a large elongated air pocket is formed inside which the turbulent structures are significantly strong to overcome forces imposed by the surrounding liquid. This elongated gas pocket reaches the bottom of the domain and an annular flow is established.

The transition from annular to bubbly flow during the ramp-down phase occurs following the same physical description in accordance with the energy balance. As the gas flow rate decreases, the vortical structures inside the gas core become weaker until a certain point where they cannot resist the consolidating effect of the surface tension. Then, the bubbles start to form again. To quantify this physical explanation, we focus on the total energy of the vortical structures in each phase. A macroscopic measure to assess the global intensity of the turbulence is enstrophy ($\Omega = \frac{1}{2}\omega \cdot \omega$, where $\omega = \nabla \times \mathbf{U}$ is the vorticity vector). The enstrophy represents the strength of the vorticity field and in other words, indicates how energetic the vortical structures are. We computed the domain-integrated enstrophy in both phases ($\langle\Omega\rangle = \int_V \frac{1}{2}\alpha_\mathrm{i}|\nabla \times \mathbf{U}|^2 dv$). **Figure** 7a displays the temporal variation of the enstrophy for the whole simulation time at each phase. The trend of variation is consistent with the aforementioned portrayal of the transition.

Initially for $t < 1$ s, the enstrophy in gas is lower than in liquid and the total vortical energy in gas could only afford to make small bubbles. Once the ramp-up phase starts, the gas enstrophy increases until $t = 3$ s, where it overcomes the liquid enstrophy (i.e., transition point). At this point, the enstrophy in liquid also grows until a certain level but remains much below gas enstrophy. Eventually, at $t = 4.2$ s the total gas enstrophy becomes more than twice the liquid enstrophy, and the annular flow is established. A similar trend holds during the ramp-down phase. The transition from annular regime to bubbly regime occurs as soon as the gas enstrophy reduces abruptly and goes below the liquid one at around $t = 9$ s.

Similarly to the way that we present the data in Figure 5b, we replotted the enstrophy data for $6 < t < 11$ s. Figure 7b demonstrates that a clear hysteresis in the transition region (i.e., where the gas enstrophy overcomes the liquid enstrophy) is observed. It is evident that there is a hysteresis in the temporal variation of the enstrophy, and further analysis on the mechanisms of enstrophy generation during the ramp-up and ramp-down in cocurrent flow is required to explain the hysteresis effect more precisely.

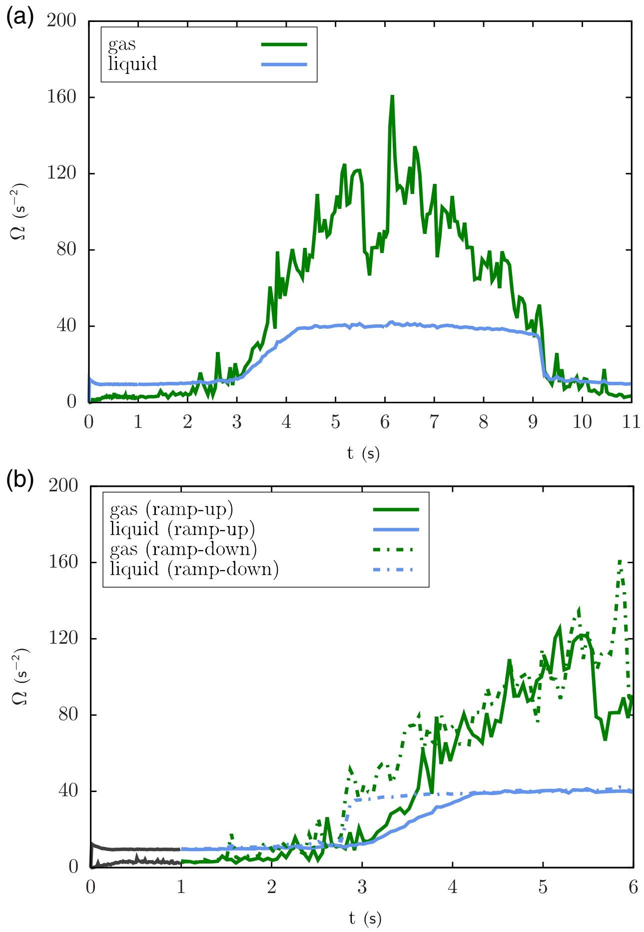

Figure 7. a) The temporal variation of domain-integrated enstrophy in each phase and b) the same plot with the rearranged ramp-down data for comparison.

3.2. Analysis of the Hysteresis

With the macroscopic analysis based on enstrophy, we could connect the regime transition in cocurrent liquid–gas flow and its hysteresis to the strength of vortical structures and the competition between the total vortical energy in each phase. As the enstrophy is proportional to the vorticity, the hysteresis should be explained by the difference in the vorticity generation/destruction mechanisms.

3.2.1. Vorticity and Enstrophy Transport Equations

By the definition, vorticity is the curl of velocity vector $\omega = \nabla \times \mathbf{U}$. Thus, by taking curl of Equation (2), the vorticity transport equation for two-phase flows is derived, which reads[23]

$$\frac{\partial \omega}{\partial t} + (U \cdot \nabla)\omega = (\omega \cdot \nabla) U + \frac{\mu}{\rho}\nabla^2 \omega \\ \underbrace{-\frac{1}{\rho^2}\nabla\rho \times \nabla \cdot (2\mu \mathbf{D})}_{T_\mu} + \underbrace{\frac{1}{\rho^2}(\nabla\rho \times \nabla p)}_{T_p} + \underbrace{\frac{\sigma}{\rho}(\nabla\kappa \times \nabla\alpha)}_{T_\sigma} \quad (4)$$

The first two terms on the right-hand side are the vortex stretching (S_ω) and dissipation of vorticity (D_ω), which are in common with the vorticity transport equation in single-phase flows. In the absence of compressibility effects, there exist three additional terms because of the two-phase nature of the flow. These terms indicate the vorticity production/destruction rates due to the misalignment between the gradient vectors. T_μ is the vorticity dissipation due to misalignment between density gradient and viscous stresses, and in fact it dissipates vorticity through the action of interfacial shear.[24] T_p is the baroclinic effects arising from the misalignment of the density and pressure gradients. T_σ is independent of the density gradient and arises due to misalignment of the gradient of curvature and gradient of volume fraction. This term generates tangential vorticity at the interface region through variations of interface curvature.[24]

As $\Omega = \frac{1}{2}\omega \cdot \omega$, the enstrophy transport equation is derived by making the scalar product of ω and Equation (4).[25] Consequently, all the mechanisms on the right-hand side of the vorticity transport equation contribute to the generation/destruction of enstrophy. For the sake of simplicity, we do not repeat the entire equation here and only evaluate each term as the scalar product of each term by the vorticity vector.

3.2.2. Discussion on the Enstrophy Generation Mechanisms

To explain the hysteresis in the total distribution of the vortical energy in the cocurrent flow, we evaluate the role of different mechanisms in the enstrophy equation. For each term, we compute the domain-integrated values normalized by the total enstrophy. We only study the gas phase because usually vorticity generation is stronger on the phase with lower density.[25] For better presentation of the results, 1) we plotted both ramp-up and ramp-down results on the same horizontal axis similar to Figure 5b and 7b and 2) we only focus on the variation rate of each mechanism, and thus, the quantities are made dimensionless with the mean values during the initial phase (denoted by subscript I).

Figure 8 displays the temporal variation of the enstrophy generation by vortex stretching term $\langle \omega \cdot S_\omega \rangle$ and enstrophy dissipation $\langle \omega \cdot D_\omega \rangle$. It is evident that the vortex stretching mechanism has an increasing rate over time and reveals no hysteresis during the ramp-up and ramp-down. Particularly, at $3 < t < 4.2$ s, where the transition happens, no distinct change in the total stretching rate is observed. The viscous dissipation $\langle \omega \cdot D_\omega \rangle$ has also an increasing (negative) effect term, which implies that the turbulence in the gas phase encounters stronger stretching and dissipation during annular flow. However, unlike the stretching term, the variation of $\langle \omega \cdot D_\omega \rangle$ exhibits several differences between the ramp-up and ramp-down. In particular, slightly before and during the transition for ramp-up (i.e., $2 < t < 4$ s) total dissipation rate remains stronger compared with the ramp-down phase. This turbulent cocurrent flow is mainly driven by the increase/decrease in the gas volume flow rate, and the main mechanism for the turbulent and vortical energy transfer across the scales is vortex stretching which shows no hysteresis. It can be concluded that the source of hysteresis in the energy of vortical structures remains independent from the inflow condition, as the inflow conditions vary similarly

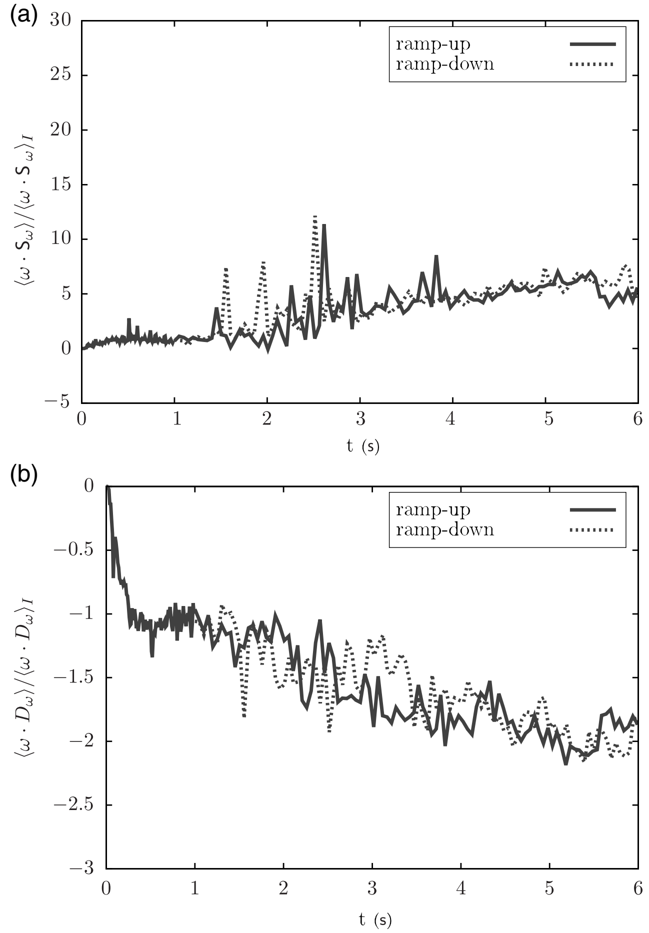

Figure 8. Temporal variation of the dimensionless domain-integrated values enstrophy generation/destruction mechanisms: a) vortex stretching term ($\omega \cdot S_\omega$) and b) dissipation term ($\omega \cdot D_\omega$).

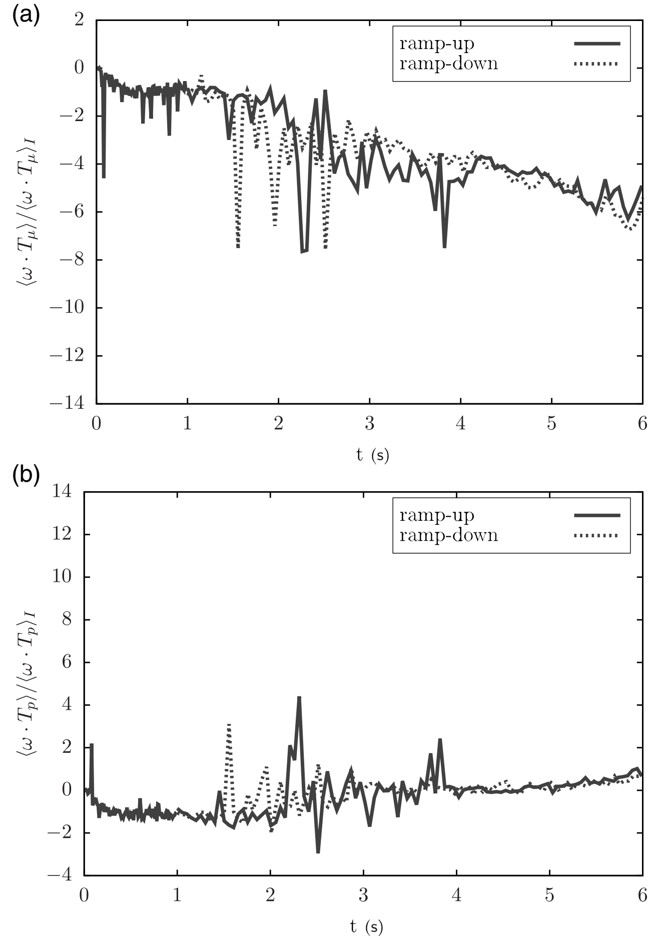

Figure 9. Temporal variation of the dimensionless domain-integrated values of misalignment terms: a) viscous dissipation term ($\omega \cdot T_\mu$) and b) baroclinic term ($\omega \cdot T_\mathrm{p}$).

according to Figure 2. Therefore, there must exist extra mechanisms for enstrophy generation during the ramp-up which are absent during the ramp-down. This is also implied by the stronger dissipation during the ramp-up because the dissipation mechanism could be interpreted as the response to the generation of enstrophy, and if the vortex stretching remains almost the same during the ramp-up and ram-down, other mechanisms should be investigated as the possible sources of hysteresis. This leads to the analysis of the three misalignment terms in enstrophy, that is, $\langle \omega \cdot T_\mu \rangle$, $\langle \omega \cdot T_\mathrm{p} \rangle$, and $\langle \omega \cdot T_\sigma \rangle$.

Figure 9 presents the temporal variation of the baroclinic and viscous misalignment terms. $\langle \omega \cdot T_\mu \rangle$ demonstrates an increasing negative effect. It dissipates enstrophy due to the misalignment between density gradient and viscous stresses which is stronger in annular flow. However, it shows almost no difference between ramp-up and ramp-down during the annular regime; there are several instants during the bubbly regime and transition (i.e. $1 < t < 4$ s) where this term reveals fluctuating behavior, leading to a discrepancy between ramp-up and ramp-down rates. $\langle \omega \cdot T_\mathrm{p} \rangle$ shows a constant rate for both regimes. It yields some negative effect at the beginning of the ramp-up (i.e., $1 < t < 2$ s) which is followed by some fluctuating values around zero during the transition; however, its total contribution to the enstrophy generation remains almost zero during the annular regime. Because the pressure jump across the liquid–gas interface is mainly aligned with a density gradient, but the dynamic variation of pressure in bubbly flow may still cause misalignment with density gradient[23] and consequently dissipates enstrophy, which is not the case for annular flow. As evident from Figure 9b, the fluctuating variation of $\langle \omega \cdot T_p \rangle$ is less pronounced during the ramp-down. Therefore, a clear conclusion remains elusive on the impact of these two misalignment terms on the occurrence of the hysteresis phenomenon.

It remains to evaluate the surface tension misalignment term. **Figure 10** demonstrates the temporal variation of $\omega \cdot T_\sigma$, which demonstrates a distinct hysteresis. As explained before, this term generates tangential vorticity due to the misalignment between the gradients of interface curvature ($\nabla\kappa$) and volume fraction ($\nabla\alpha$), and this enstrophy generation mechanism is solely dependent on the interface topology. As evident from Figure 10, it is initially large for bubbly flow because the higher

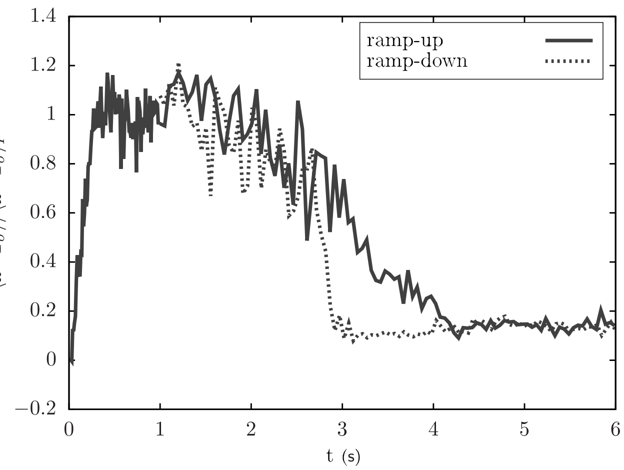

Figure 10. Temporal variation of the dimensionless domain-integrated surface tension misalignment term $(\omega \cdot T_\sigma)$.

variations of the interface curvature lead to larger $\nabla\kappa \times \nabla\alpha$. When ramp-up begins, it starts to decrease and reduces significantly during the transition until it reaches almost 10% of its initial value at $t = 4.2$ s. At this moment, the annular flow is established, and this source of enstrophy production remains constantly low, as $\nabla\kappa$ tends to zero.

The ramp-down begins while this term has its minimum effect. In the absence of flow disturbance, this term remains at the lowest level for a longer time, and consequently, the annular regime lasts longer, even though the transition to the bubbly regime is expected at a similar time to the ramp-down. From a microscopic point of view, $\nabla\kappa \times \nabla\alpha$ generates tangential vortical structures in the vicinity of the liquid–gas interface that counteract the vortical structures generated by the vortex stretching mechanism. Hence, it could be interpreted as the resistance of the liquid–gas interface to the bulk gas flow. During the ramp-down (starting from the annular regime), and in the absence of these vortical structures at the interface, the resistance of the liquid–gas interface against the gas is lower, and therefore the annular flow has the tendency to remain intact for a longer time. This physical explanation is also consistent with the lower amount of enstrophy dissipation (Figure 8b); however, such detailed analysis on the interaction of vortical structures requires fully resolved simulation data and therefore remains out of the scope of this article. Based on the macroscopic analysis in this work, we can conclude that as $\omega \cdot T_\sigma$ is majorly determined by the interface topological changes, its temporal variation would be dependent on the history of the interfacial flow structures. Therefore, the hysteresis phenomenon may be explained by the differences in the history of the interfacial flow and this mechanism during the ramp-up and ramp-down, that is, $\langle\omega \cdot T_\sigma\rangle_{\text{ramp-down}} \ll \langle\omega \cdot T_\sigma\rangle_{\text{ramp-up}}$.

3.2.3. Implication of Findings to the SEN Flow in Continuous Casting

The argon gas injection during the continuous casting process could potentially constitute a cocurrent downward liquid–gas flow in the SEN. The argon is injected through a complex nozzle geometry in real-scale SEN, and the liquid flow rate varies by the adjustment of stopper position.[16] As mentioned in the introduction, the annular regime has to be prevented for a sustainable steel-making process. Thus, a clear picture of the phase distribution in the SEN and an in-depth physical understanding of the hysteresis phenomenon in regime transition are of great importance when varying the operating conditions. The proposed simulation setup is much simpler than the real-scale SEN flow as the gas injection is resembled by explicit source terms in the computational domain (which entails the limitations to reach a dense bubbly flow with several small bubbles, as may be expected in the real SEN). Nevertheless, the physical core concept and the proposed macroscopic analysis based on the enstrophy in interfacial flow would remain relevant to SEN flow. In other words, the present study connects the hysteresis phenomenon to the history of interfacial structures and the state of vortical energy level produced by each physical mechanism. Therefore, the initiation of bubbly-to-annular transition would occur at different enstrophy levels compared with the annular-to-bubbly transition. This could be a key parameter in SEN flow control and process operation plans.

4. Conclusion

The present study investigates the regime transition and the hysteresis effect in downward liquid–gas flows using multiphase CFD simulation. We proposed a workable simulation setup for the cocurrent flows with varying operating conditions. A vertical pipe with a turbulent water inlet is considered at the top of which the gas is injected as a time-varying volumetric source in the VOF transport equation. This setup enables us to realize the linear increase and decrease in gas flow rate similar to water model experiments. The numerical simulations were performed using the geometric VOF solver of OpenFOAM. The simulations are capable of picturing different regimes and the transition between bubbly and annular flows. The results also exhibit hysteresis in transition points during the ramp-up and ramp-down phases. Based on the instantaneous snapshots of the interfacial and vortical structures, we could come up with a physical description for the regime transition based on the vortical energy balance. We further quantified this energy balance by comparing the domain-integrated enstrophy in each phase. The analysis connects the regime transition to the evolution of interfacial turbulence by analyzing the total vortical energy of the turbulent structures and the mechanisms that contribute to the distribution of enstrophy in each phase. We analyzed the temporal variation of different terms in the enstrophy transport equation and the following conclusions are drawn for the hysteresis in regime transition. 1) The hysteresis in regime transition is found to be independent of the inflow condition and is mainly driven by the local interfacial topological changes. 2) The hysteresis phenomenon may be explained by the differences in the history of the interfacial structures during ramp-up and ramp-down that entail vorticity/enstrophy generation at different energy levels upon transition.

Based on the macroscopic analysis of enstrophy generation, this study provides insights into the regime transition of cocurrent flow in SEN and could be used as a basis for further investigation in steel quality control.

Acknowledgements

The authors acknowledge the funding support of K1-MET GmbH, metallurgical competence center. The research programme of the K1-MET competence center is supported by Competence Center for Excellent Technologies (COMET), the Austrian programme for competence centers. COMET is funded by the Federal Ministry for Climate Action, Environment, Energy, Mobility, Innovation and Technology, the Federal Ministry for Digital and Economic Affairs, the Federal States of Upper Austria, Tyrol and Styria, as well as the Styrian Business Promotion Agency (SFG). Besides the public funding from COMET, this research project was partially financed by the scientific partner Johannes Kepler University Linz and the industrial partner RHI Magnesita.

Conflict of Interest

The authors declare no conflict of interest.

Data Availability Statement

The data that support the findings of this study are available from the corresponding author upon reasonable request.

Keywords

enstrophy, liquid–gas flows, submerged entry nozzles, transitions, volume of fluid method

Received: December 10, 2021
Revised: January 21, 2022
Published online: March 7, 2022

[1] P. Planquart, S. Dehaeck, J.-M. Buchlin, M. Riethmuller, in *5th Int. Conf. on Multiphase Flow, ICMF 2004*, Yokohama, Japan, May 2004.
[2] A. Ramos-Banderas, R. Morales, R. Sanchez-Perez, L. Garcia-Demedices, G. Solorio-Diaz, *Int. J. Multiphase Flow* **2005**, *31*, 643.
[3] T. Oshinowo, M. E. Charles, *Can. J. Chem. Eng.* **1974**, *52*, 25.
[4] T. Oshinowo, M. E. Charles, *Can. J. Chem. Eng.* **1974**, *52*, 438.
[5] M. Ishii, S. Paranjape, S. Kim, X. Sun, *Int. J. Multiphase Flow* **2004**, *30*, 779.
[6] J. Y. Lee, M. Ishii, N. S. Kim, *Int. J. Heat Mass Transfer* **2008**, *51*, 3442.
[7] J. Enrique Julia, Y. Liu, T. Hibiki, M. Ishii, *Exp. Therm. Fluid Sci.* **2013**, *44*, 345.
[8] B. Wu, M. Firouzi, T. Mitchell, T. E. Rufford, C. Leonardi, B. Towler, *Chem. Eng. J.* **2017**, *326*, 350.
[9] D. Barnea, O. Shoham, Y. Taitel, *Chem. Eng. Sci.* **1982**, *37*, 741.
[10] D. Barnea, *Int. J. Multiphase Flow* **1986**, *12*, 733.
[11] Z. Yang, Z. Dang, X. Yang, M. Ishii, J. Shan, *Int. J. Heat Mass Transf.* **2018**, *125*, 179.
[12] Z. Li, G. Wang, M. Yousaf, X. Yang, M. Ishii, *Int. J. Heat Mass Transf.* **2018**, *118*, 812.
[13] M. Lokanathan, T. Hibiki, *Prog. Nucl. Energy* **2018**, *103*, 165.
[14] K. Usui, *J. Nucl. Sci. Technol.* **1989**, *26*, 1013.
[15] T. Maruyama, S. Yoshida, T. Mizushina, *J. Chem. Eng. Jpn.* **1981**, *14*, 352.
[16] M. Thumfart, G. Hackl, W. Fellner, in *9th Int. Conf. on Modeling and Simulation of Metallurgical Processes in Steelmaking - STEELSIM2021*, Austria **2021**.
[17] J. Brackbill, D. Kothe, C. Zemach, *J. Comput. Phys.* **1992**, *100*, 335.
[18] J. Roenby, H. Bredmose, H. Jasak, *R. Soc. Open Sci.* **2016**, *3*, 160405.
[19] M. Saeedipour, S. Vincent, J.-L. Estivalezes, *Acta Mech.* **2021**, *232*, 2695.
[20] M. Saeedipour, S. Schneiderbauer, *Int. J. Multiphase Flow* **2021**, *144*, 103780.
[21] OpenCFD, *OpenFOAM - The Open Source CFD Toolbox - User's Guide*, OpenCFD Ltd., v2006 edition, **2020**.
[22] M. Saeedipour, S. Vincent, S. Pirker, *Int. J. Multiphase Flow* **2019**, *112*, 286.
[23] J. Hasslberger, M. Klein, N. Chakraborty, *J. Fluid Mech.* **2018**, *857*, 270.
[24] J. Magnaudet, M. J. Mercier, *Annu. Rev. Fluid Mech.* **2020**, *52*, 61.
[25] Z. Li, F. A. Jaberi, *Phys. Fluids* **2009**, *21*, 095102.